Mechanical interpretation of dry granular masses impacting on rigid obstacles

Francesco Calvetti[1] · Claudio di Prisco[1] · Irene Redaelli[1] · Anna Sganzerla[1] · Emmanouil Vairaktaris[2]

The evaluation of impact forces exerted by flowing granular masses on rigid obstacles is of fundamental importance for the assessment of the associated risk and for the design of protection measures. Empirical formulae are available in the literature estimating the maximum impact force; most of them are based on over-simplifying hypotheses about the behaviour of the granular material. For practical applications, formulations based on either hydrodynamic or elastic body models are often employed. These formulations require the use of empirical correcting factors. In this paper, the same DEM method is used to investigate the relationship between the evolution with time of the impact force and the micromechanics of the granular mass. In fact, considering the dynamic nature of impacts, the impulse value is fundamental for the dynamic response of the barrier, and the mere information about the maximum impact force is not sufficient to design protection works, or assess the vulnerability of structures. Information about contact forces and particle velocities will be discussed and critically compared with macroscopic results. In order to progressively introduce the complexity of the impact phenomenon, four geometrical and mechanical conditions are considered: (a) vertical front, confined flow, bonded material; (b) vertical front, confined flow, purely frictional material; (c) vertical front, free surface flow, purely frictional material; (d) inclined front, free surface flow, purely frictional material.

Keywords DEM · Dry granular media · Impact · Sheltering structures

1 Introduction

The design of shelters for rapid landslide risk mitigation is based on the evaluation of the force exerted on them by the flowing material. Considering the dynamic nature of impacts, the evolution with time of the impact force should be used in design. However, in most practical approaches and standards, a pseudo-static approach is very often considered: the maximum impact force is estimated by using empirical formulae and is quasi-statically applied to the barrier. These empirical formulae are based on either hydrostatic [4, 17, 18, 27, 28], hydrodynamic [3–5, 14, 16, 17, 21, 28, 31], hybrid [3, 13, 17] or boulder impact theories [14, 17, 20, 21] and when used to match real case histories, require the introduction of highly dispersed empirical coefficients [8, 9]. For this reason, their application for prediction and design is highly questionable.

In order to highlight and overcome the limitations of these approaches, the DEM has been largely employed to simulate the impact of dry granular flows on rigid obstacles and to evaluate accurately the value of the impact force. In particular, Teufelsbauer [30] observed that the DEM represents a suitable numerical tool for the simulation of such phenomena, and good agreement between laboratory and DEM numerical results can be obtained. In Shen et al. [29],

Received: 27 November 2018
Accepted: 30 May 2019

✉ Irene Redaelli (irene.redaelli@polimi.it)
Francesco Calvetti (francesco.calvetti@polimi.it)
Claudio di Prisco (claudio.diprisco@polimi.it)
Anna Sganzerla (anna.sganzerla@mail.polimi.it)
Emmanouil Vairaktaris (mvairak@mail.ntua.gr)

[1] Politecnico di Milano, Milan, Italy
[2] National Technical University of Athens, Athens, Greece

the DEM was employed to study accurately the dynamic interaction between an inclined barrier and the granular flow as well as the energy dissipation mechanisms during the impact. In Albaba et al. [1], the variation of the impact force values along the height of the rigid obstacle has been studied. In order to better understand the impact mechanics, very recently, the authors have performed an extensive numerical campaign by using a discrete element (DEM) 3D model [7]. A number of design factors determining the impact force, namely the geometry of the sliding mass (length, width and flow height, inclination of the front) and the impact velocity, have been considered. The simulations also allowed assessing the effect of other relevant parameters such as the velocity profile along the vertical and the granular mass porosity. On the other hand, the sand friction angle does not significantly influence the value of the maximum impact force [10, 23].

In the simulations, only the mere impact is considered, while the propagation phase is disregarded. Therefore, the model is generated just in front of the obstacle with the chosen geometry and properties, and impact velocity is imposed as initial condition. In this paper, the same approach is adopted, see Sect. 2 for further details. Such approach has the advantage of precisely defined impact conditions, which is necessary for a reliable interpretation of the results. On the negative side, the impact conditions may seem somehow artificial, in that they are not the outcome of a runout simulation performed on the same material. However, the extent of the study covers the range of data reported from the observation of real debris flow events [2, 7, 15, 24, 26] in terms of impact velocity (4–50 m/s), velocity profile (constant, linear, parabolic), mass porosity (0.45–0.65), front inclination (30–90°) and flow height (1.5–7.5 m). Ahmadipur and Qiu [2] demonstrated, through a series of 2D flume laboratory tests, that the velocity of the flow at the impact time can be inferred from the slope angle, the sliding distance and the initial density of the mass, since these quantities have an effect on the initial potential energy, converted into kinetic energy during the propagation stage. Nevertheless, the role of granular temperature/velocity fluctuations, although the authors are perfectly aware of its importance [25], is hereafter, for the sake of simplicity, disregarded.

The results have been so far interpreted from a macroscopic point of view in terms of maximum impact force. A new design formula has been introduced accordingly, and the maximum average dynamic pressure (Δp_{MAX}) exerted by the granular mass has been written as:

$$\Delta p_{\max} = a_1 \frac{1}{2} \rho_s u_M u_0 + a_2 \frac{1}{2} \rho_s u_0^2 \qquad (1)$$

where u_0 is the impact velocity, u_M is the propagation velocity of compression waves within the impacting mass and ρ_s is the unit mass of the grains. The first term of Eq. 1 is linear with u_0 and depends on the stiffness and density of the material. This term corresponds to the pressure exerted by the impact of a deformable body on a rigid obstacle. The second term, independent of u_M, is quadratic with u_0 and is analogous to the dynamic pressure exerted by a fluid. The two non-dimensional coefficients a_1 and a_2, defining the relative weight of the two components, are a function of material stiffness and front inclination [7].

Although such finding is very interesting and useful from a practical point of view, the DEM model can provide much more insight into the micro-mechanism (at the scale of the grain) determining the global behaviour [12]. Moreover, information about the duration of impacts, which are dynamic phenomena, is crucial from a design point of view. For this reason, a new set of simulations have been performed and interpreted both from a micromechanical and global (macroscopic) point of view.

Even though flexible barriers are becoming popular all around the world [22], in this work, the obstacle is assumed to be rigid. With respect to flexible barriers, an upper bound of the impact force is obtained and the simpler conditions allow to study in detail the complex mechanics of the deforming granular mass during impact.

2 DEM model

The numerical simulations are performed using the code PFC3D 4.0 [19]. The geometry of the DEM model is represented in Fig. 1. As in Calvetti et al. [7], the granular mass is assumed to be dry and represented by an assembly of polydisperse spherical particles of unit weight γ_g (Table 1). A linear force–displacement contact law, set in series with a slider obeying the Coulomb's friction law in the tangential direction, has been employed. The values of the normal and shear particle stiffnesses k_n/D and k_s/D and the interparticle friction coefficient μ_g are reported in Table 1. Particle rotation has been inhibited to reproduce the response of real soils, where particles are not spherical [6, 7]. No numerical damping is used in the simulations. In order to simulate elastic impacts (Sect. 3.1), unbreakable normal and shear bonds (with shear and tensile strength of the order of 10^{10} kN) are added to each contact between particles, so that all sources of non-reversible deformation are inhibited. All the mechanical properties of the particles and of the assembly are listed in Table 1.

The obstacle is represented by a vertical rigid and massless wall of height $H = 6$ m and friction coefficient μ_w. The mass flows on a horizontal wall with friction μ_b. Plane strain conditions are imposed by confining the flow between two smooth lateral wall elements. The thickness of the channel is equal to 8 D, in order to prevent boundary

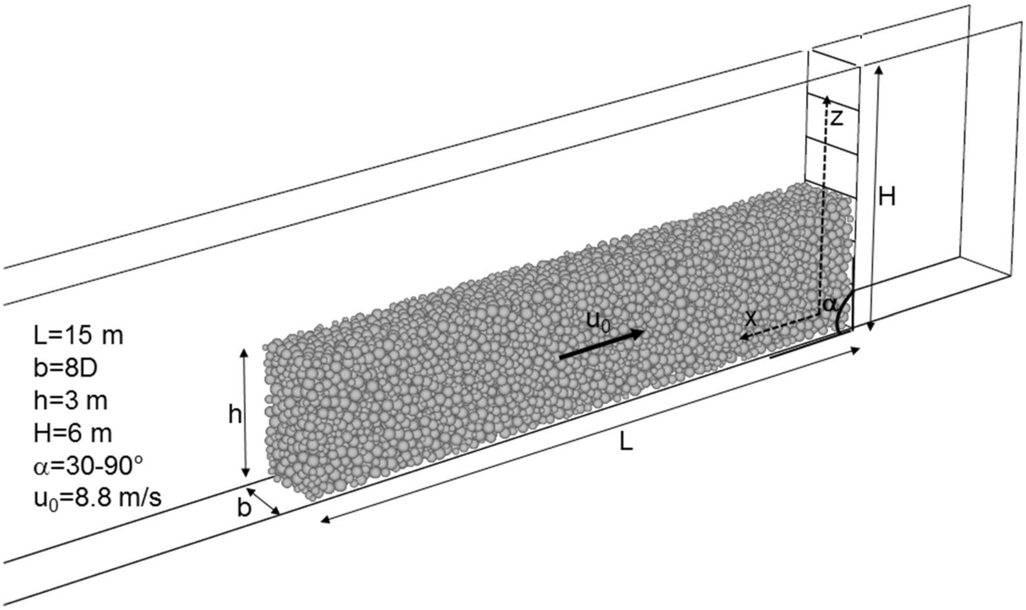

Fig. 1 3D view of the DEM model with test conditions

Table 1 Model properties

Average grain diameter, *D* (m)	0.3
$D_{\mathrm{MAX}}/D_{\mathrm{MIN}}$	2.4
Particle unit weight, γ_g (kN/m^3)	2.6
Normal contact stiffness k_n/D (MPa)	300
Shear contact stiffness k_s/D (MPa)	75
Contact friction coefficient μ_g	0.3
Base friction coefficient μ_b	0.3
Obstacle friction coefficient μ_w	0.6
Porosity	0.45
Bulk density, ρ (t/m^3)	1.43

effects and to limit the number of particles in the model [7]. In order to simulate impacts under confined conditions (see Sects. 3.1 and 3.2), a horizontal smooth rigid wall is added on the top of the model to prevent vertical displacements of particles.

2.1 Simulation procedure and analysis of results

The simulations reproduce the impact process only, while both triggering and propagation phases are disregarded.

The modelling procedure consists in the following stages:

1. The impacting granular mass is generated just in front of the obstacle with the prescribed granular size distribution. The porosity is assumed to be initially uniform within the grain mass and equal to $n = 0.45$. A discussion of the effect of initial porosity is in Calvetti et al. [7] and Ceccato et al. [10].
2. The assembly is relaxed under zero gravity. At the end of this stage, no contact forces are present in the granular assembly.
3. The interparticle friction, gravity and the initial impact velocity u_0 are assigned to all particles. The velocity profile is assumed to be initially uniform within the assembly. The effect of the initial velocity profile is in Calvetti et al. [7].
4. The impact is simulated and the evolution of the impact force is monitored.

Further details about the model, simulation procedure and preliminary analyses are presented in Calvetti et al. [7].

In order to interpret the results, a number of non-dimensional variables have been introduced and will be used in the following. f^* is the impact force f normalised by the static force f_s exerted on the obstacle by a fluid with a unit weight equal to the unit weight of grains ($f_s = 1/2\gamma_s h^2 b$); t^* is time t normalised by the duration t_M of the collision between two grains of diameter D and mass m_g ($t_M = \pi/\sqrt{k_N/m_g}$):

$$f^* = \frac{f}{f_s}; t^* = \frac{t}{t_M} \qquad (2)$$

3 Numerical results: vertical front

In order to progressively analyse the complexity of the impact phenomenon, four series of simulations are performed. They are characterised by the following geometrical/mechanical conditions: (a) vertical front, confined flow, elastic material; (b) vertical front, confined flow; (c) vertical front, free surface flow; (d) inclined front, free surface flow. In this section, the results of the simulations are analysed and the relationship between macroscopic results and the evolution of microscopic data (particle velocity and displacement, contact forces) is illustrated. In all simulations, reference initial conditions of Fig. 1 are adopted: flow height, $h = 3$ m; flow length $L = 15$ m; impact velocity $u_0 = 8.8$ m/s. Front inclination, α ranges between 30° and 90°.

3.1 Confined flow, bonded material

This condition corresponds to a 1D elastic impact and is the simplest from a geometrical and mechanical point of view. For this reason, in the confined case, gravity has not been introduced in the model. Although this case is not realistic, it is very useful for interpreting the underlying mechanics and for comparing the results with the theoretical elastic solution.

The trend of the impact force (Fig. 2a) is characterised by a horizontal plateau which is attained quite rapidly, followed by a rapid decrease to zero.

In Fig. 2b, the evolution of the kinetic energy (E_{kin}), the elastic stored energy (E_{el}) and the dissipated frictional energy (E_{f}) are reported, normalised with respect to the initial energy E_0 of the system. E_{kin} is computed as the sum of the kinetic energy of all particles, E_{el} is the sum of elastic energy stored in all normal and tangential contact springs and E_{f} is the time integral of the incremental work of the tangential force at all sliding contacts [19].

During the impact, the initial kinetic energy of the system ($E_{\mathrm{kin}} = E_0$) is exchanged with the elastic energy stored in contacts (E_{el}). Thanks to bonds, no energy is dissipated by contact friction ($E_f = 0$). In the first phase of the impact ($t^* < 50$), the initial kinetic energy is progressively transformed into elastic energy (Fig. 2b). Note that the storage of elastic energy takes place essentially under a constant impact force. At approximately $t^* = 50$, kinetic energy nearly nullifies (the velocity of all particles is virtually zero) and is stored in contacts. After $t^* = 50$, the stored elastic energy starts releasing transforming back into kinetic energy.

The analysis of the evolution of the field of contact forces and particle velocities during the impact is shown in Fig. 3. As the front particles hit the obstacle, a compression wave is generated. In the first phase of the impact, this wave propagates backward. Behind the front of this wave, particle velocities are zero; beyond, contact forces are zero. The transition between these two zones is quite sharp (see Fig. 4).

When the propagation wave reaches the end of the granular mass ($t^* = 50$), all particles are characterised by zero velocity and contact forces are almost uniformly distributed within the mass. From this time instant on, a tension wave is reflected from the back of the granular mass towards the obstacle. Behind the front of this wave, particles get a negative velocity (i.e. they bounce back with a velocity equal to u_0, see Fig. 4a for a quantitative evaluation) and the contact forces are virtually zero, although a disordered network of compression and tension contact forces is observed. These forces, which are due to the local heterogeneity of the granular assembly, are negligible and do not contribute significantly to the elastic energy stored in the system (see Fig. 2b). All in all, the behaviour of the mass is qualitatively similar to that of a deformable elastic body (a quantitative comparison is shown in Sect. 4.1).

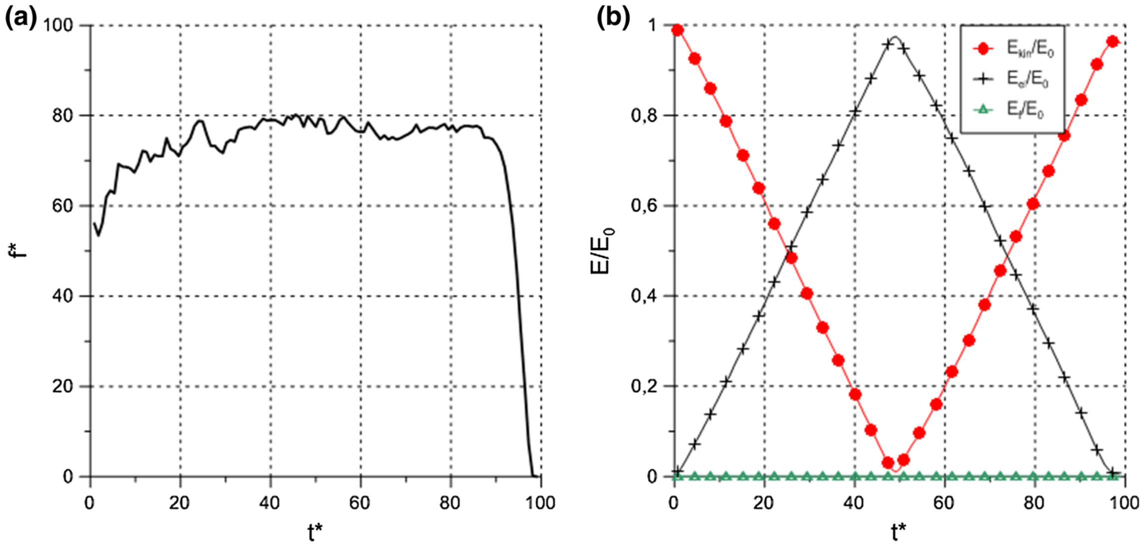

Fig. 2 Confined impact, vertical front, bonded particles. **a** Evolution of impact force; **b** evolution of energy components

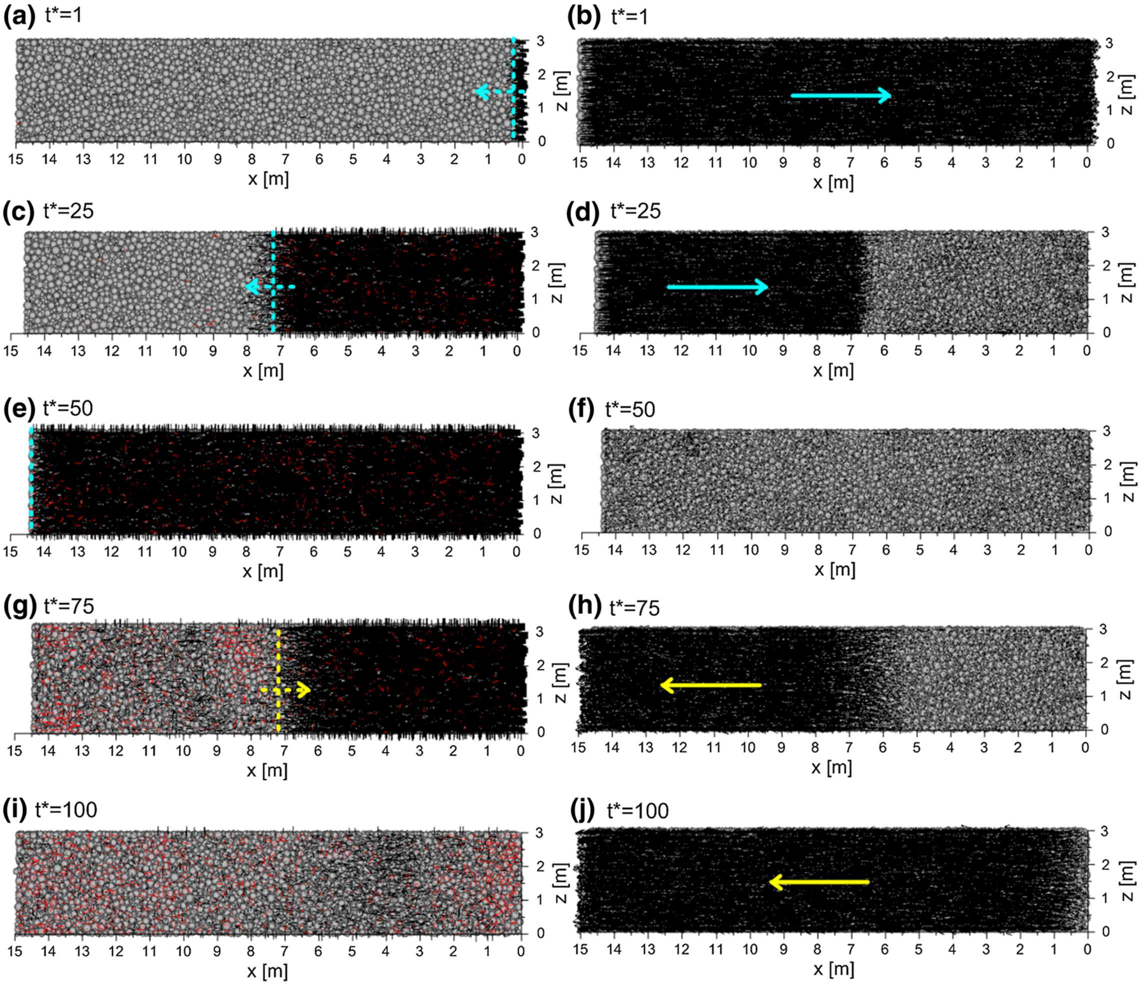

Fig. 3 Vertical front, confined flow, bonded particles. Contact forces (left) and particle velocities (right) at selected time instants. The intensity of force chains is normalised with respect to 200 kN, whereas the intensity of the velocity vectors with respect to 8.8 m/s. Black/red contact forces indicate compression/extension. Dashed arrows represent the moving direction of the wave front, whereas dashed lines represents the profile of the compression/rarefaction waves; solid arrows indicate the direction of the velocity vectors

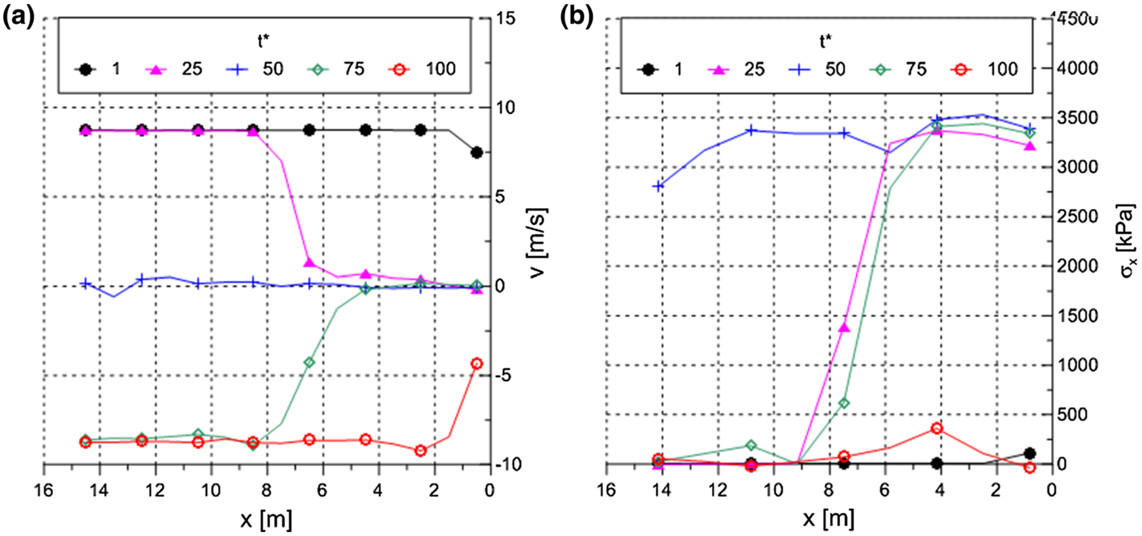

Fig. 4 Average horizontal velocity (**a**) and horizontal stress (**b**) as a function of the distance from the obstacle

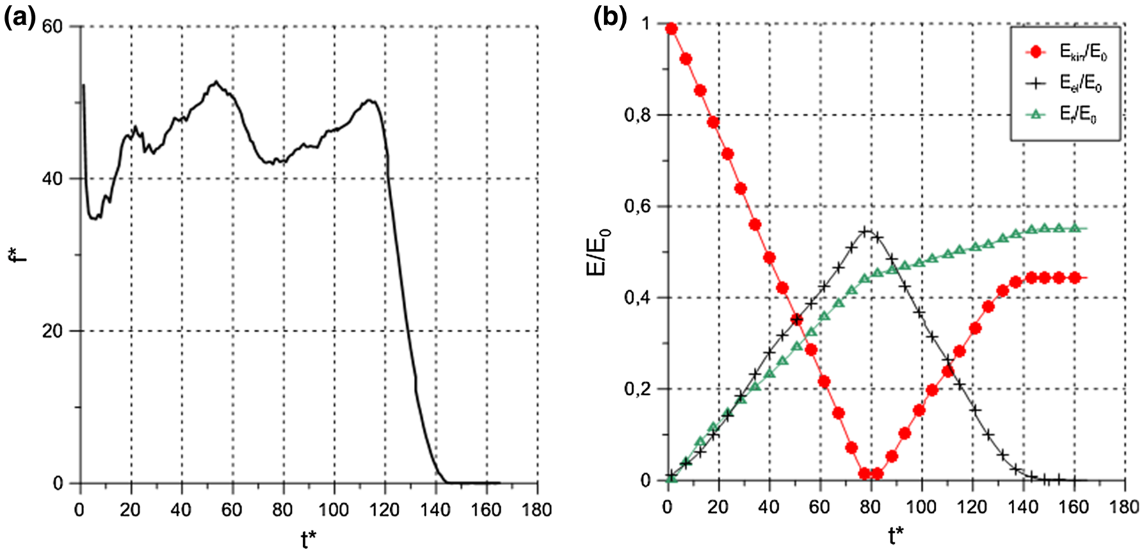

Fig. 5 Confined impact, vertical front. Evolution with time of: **a** normalised impact force; **b** normalised energy components E_{kin}, E_{el} and E_{f}

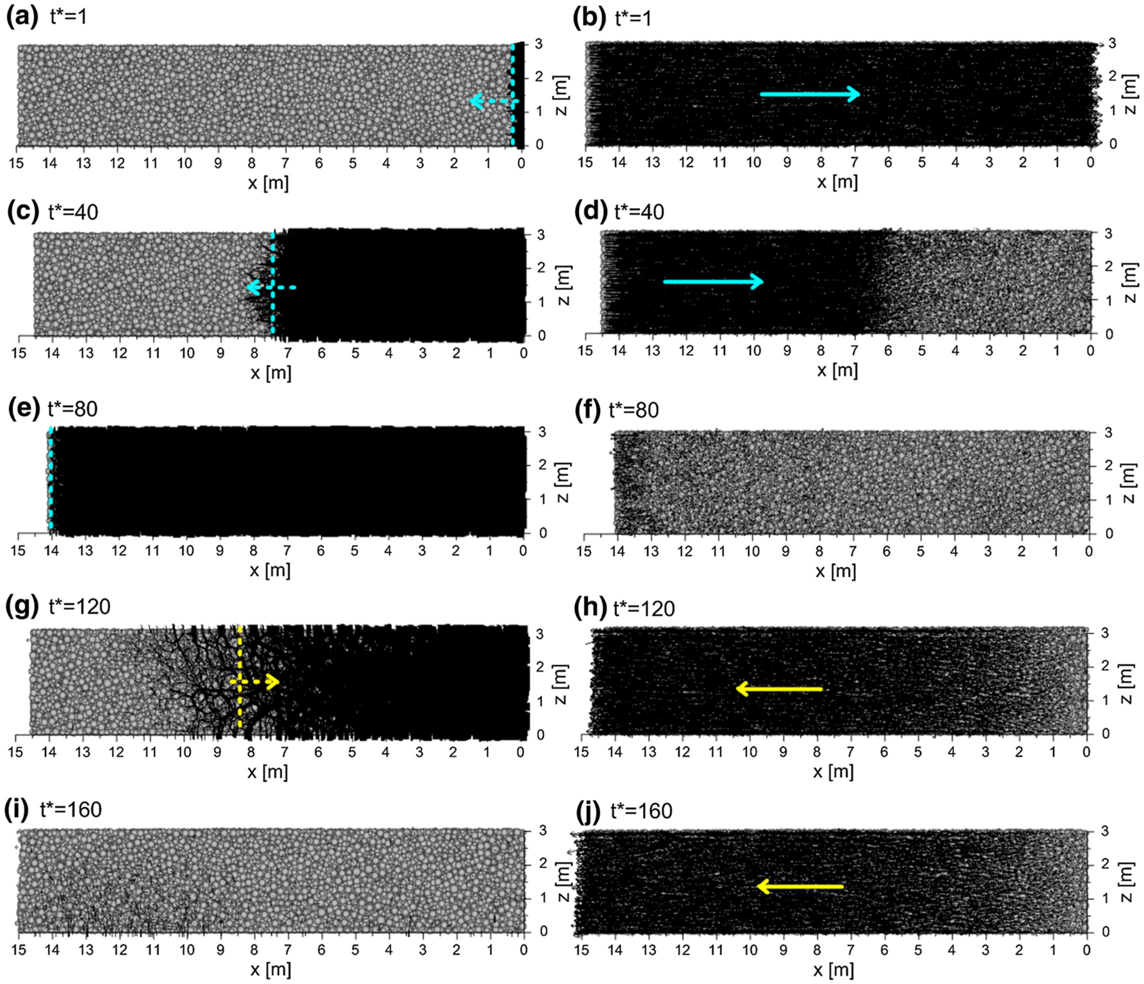

Fig. 6 Contact forces (left) and particle velocities (right) at selected time instants. Vertical front, confined flow. The intensity of force chains is normalised with respect to 200 kN, whereas the intensity of the velocity vectors with respect to 8.8 m/s. Dashed arrows represent the moving direction of the wave front, whereas dashed lines represents the profile of the compression/rarefaction waves; solid arrows indicate the direction of the velocity vectors

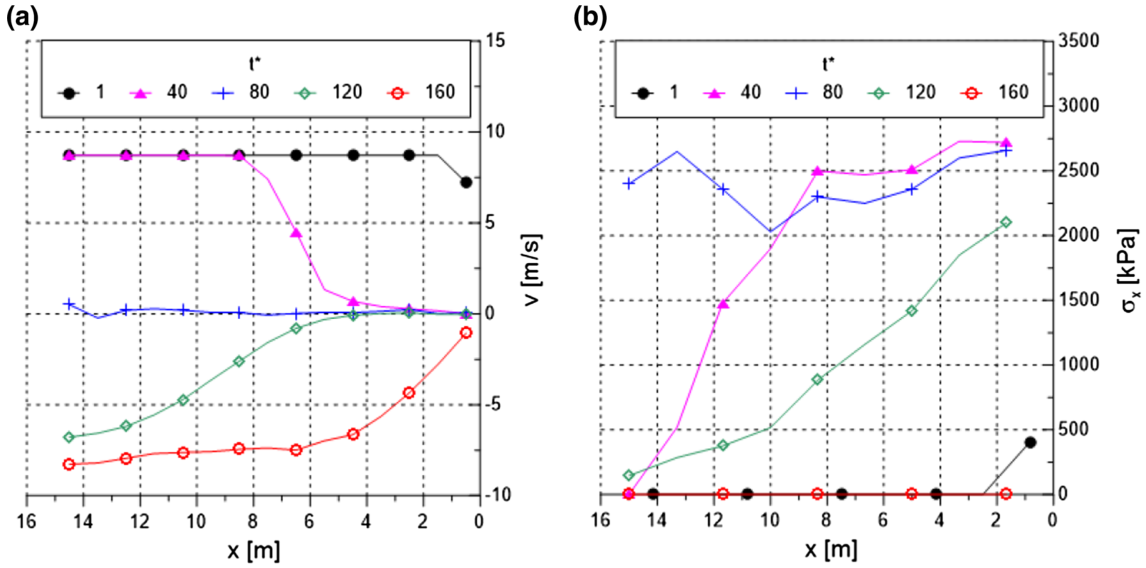

Fig. 7 Average horizontal velocity (**a**) and horizontal stress (**b**) as a function of the distance from the obstacle

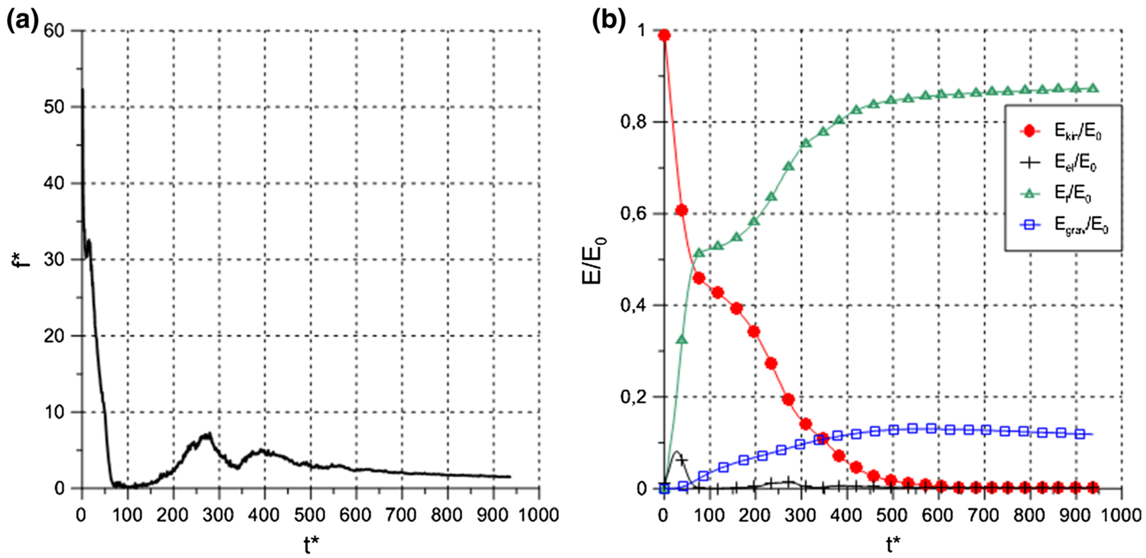

Fig. 8 Vertical front, free surface. Evolution with time of: **a** normalised impact force; **b** normalised energy components E_{kin}, E_{el}, E_{f} and E_{grav}

Starting from the data plotted in Fig. 3, average values of velocities and forces can be calculated for particles and contacts belonging to vertical slices. 1 m wide slices are chosen to get both sufficient detail and reliable averages. Average horizontal stresses are then calculated from contact forces by using a homogenisation procedure [19]. The profiles of average horizontal particle velocities and average horizontal stresses, as a function of the distance to the obstacle, are plotted in Fig. 4 and confirm the previous qualitative observations. In particular, it is evident that particle velocity is zero between the front of the impact wave and the barrier, and equal to the impact velocity in the remaining region between the wave front and the back of the mass. Moreover, the magnitude of impact and rebound velocities is the same.

Horizontal stresses are quite uniform and constant between the front of the impact wave and the barrier, and nearly zero between the wave front and the back of the mass. The average value of the impact stress is between 3 and 3.5 MPa (cfr. Sect. 4.1). From the analysis of Fig. 4, it is also possible to evaluate in approximately 2 m the thickness of the transition zone around the impact wave front position.

3.2 Confined flow, frictional material

In order to highlight the influence of particle sliding within the granular mass, a second simulation is performed

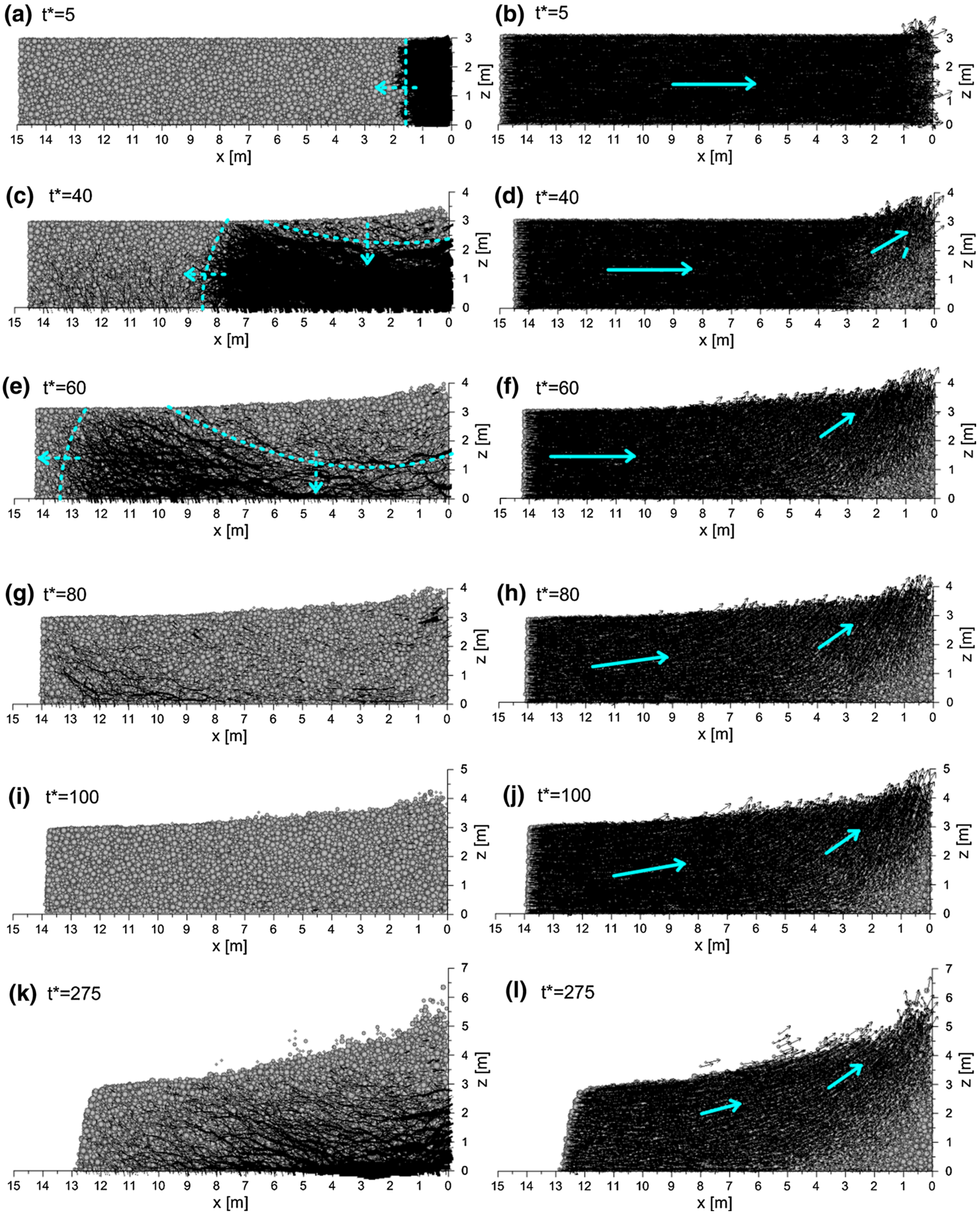

Fig. 9 Contact forces (left) and particle velocities (right) at selected time instants. Vertical front, free flow. The intensity of force chains is normalised with respect to 200 kN, whereas the intensity of the velocity vectors with respect to 8.8 m/s. Dashed arrows represent the moving direction of the wave front, whereas dashed lines represents the profile of the compression/rarefaction waves; solid arrows indicate the direction of the velocity vectors

without adding contact bonds under the same conditions (vertical front, confined flow). The expected behaviour of the granular mass is that of a purely frictional material and, under conditions similar to oedometric, plastic deformations are expected to develop.

The evolution of the impact force (Fig. 5a) is qualitatively similar to that obtained in previous elastic case (Fig. 2a), but the maximum value of the impact force is much smaller, and the duration of the impact is longer. The initial kinetic energy is now both progressively transformed into elastic energy (i.e. stored in the contacts) and dissipated by contact friction (Fig. 5b). In the second phase of the impact, the stored elastic energy is released and transformed back into kinetic energy and dissipated. However, as a result of energy dissipation, the final (rebound) value of kinetic energy is smaller than the initial one. Note that the rate of energy dissipation is different during loading and unloading phases.

In terms of contact forces and particle velocities (Fig. 6), the first phase of the impact is qualitatively similar to that of the bonded material, although the velocity of propagation of the impact wave is smaller (a quantitative interpretation is given in Sect. 4.1). From the time instant when the impact wave reaches the back of the mass (t* = 80), a no-tension wave is reflected from the back of the granular mass towards the obstacle. Behind the front of this wave, particles get a negative velocity (i.e. they bounce back, with a velocity smaller than u_0 because of energy dissipation) and the contact forces network is completely disrupted. All in all, the behaviour of the mass seems to be very similar to that of a deformable elasto-plastic (with tension cut-off) body.

The profiles of average horizontal particle velocities and average horizontal stresses (Fig. 7) are similar to that obtained in the bonded case. However, some quantitative differences are evident. First of all, the impact stress (between 2 and 2.5 MPa in this case) is smaller. As already observed, the rebound velocity is smaller than the impact velocity. Moreover, the extension of the transition zone across the front of the impact waves is larger, especially during the rebound phase, which indicates a progressive increase in agitation (velocity fluctuations) within the system. This tendency is particularly evident during the unloading phase. Note that these fluctuations are not associated with an increase in the energy dissipation rate (Fig. 5b) as one might expect. This is due to the fact that the structure of the mass is disrupted in tension (no energy dissipation involved) because of the unbonded nature of the material, and the number of contacts decreases dramatically.

3.3 Free surface flow, frictional material

This simulation is performed without the confining (top) wall, which allows particles to expand vertically during the impact.

The effect of removing the confined flow constraint is evident by comparing Figs. 5 and 8. With the exception of the very first instants, there are both qualitative and quantitative differences between the two conditions: in the unconfined case, the impact force decreases very rapidly from the initial value to zero and is characterised in the following by an irregular trend with two sub-peaks; eventually the impact force decreases to a residual value. Despite the rapid impact force decrease, the duration of the impact is much longer in the unconfined case, and energy dissipation is much larger. In quantitative terms, the stored elastic energy never exceeds 10% of the impact energy (see Sect. 4 for a more detailed analysis). At the end of the impact, all kinetic energies have been either dissipated within the granular mass or transformed into potential gravitational energy (E_{grav}) as a consequence of the vertical expansion of the mass). Shen et al. [29] also observed that after the impact, most of the initial energy is dissipated by interparticle friction within the granular mass and by particle–base friction, whereas the elastic strain energy is negligible.

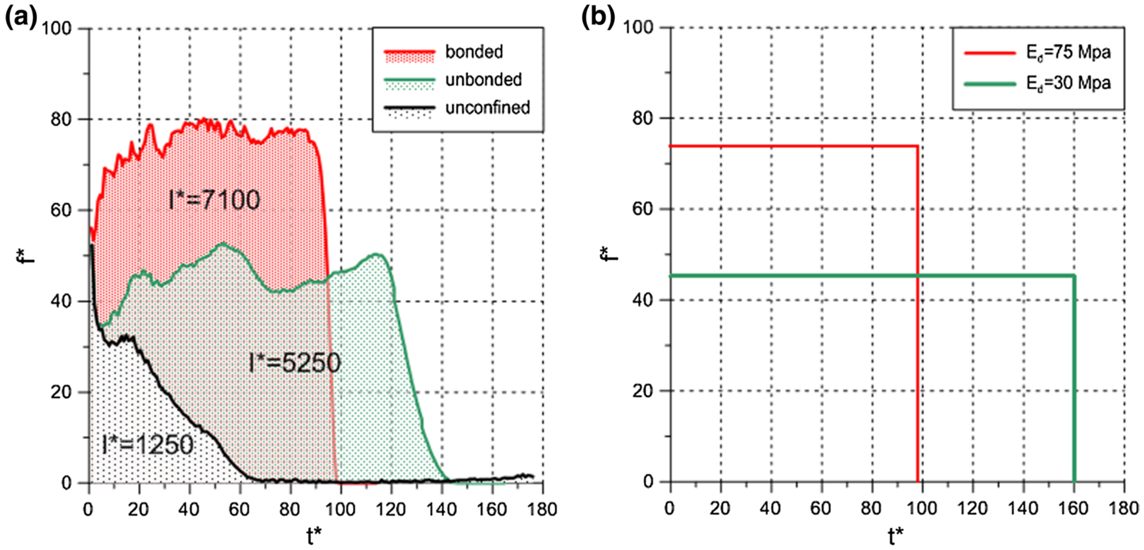

Fig. 10 Evolution of impact forces. **a** numerical results; **b** deformable body impact

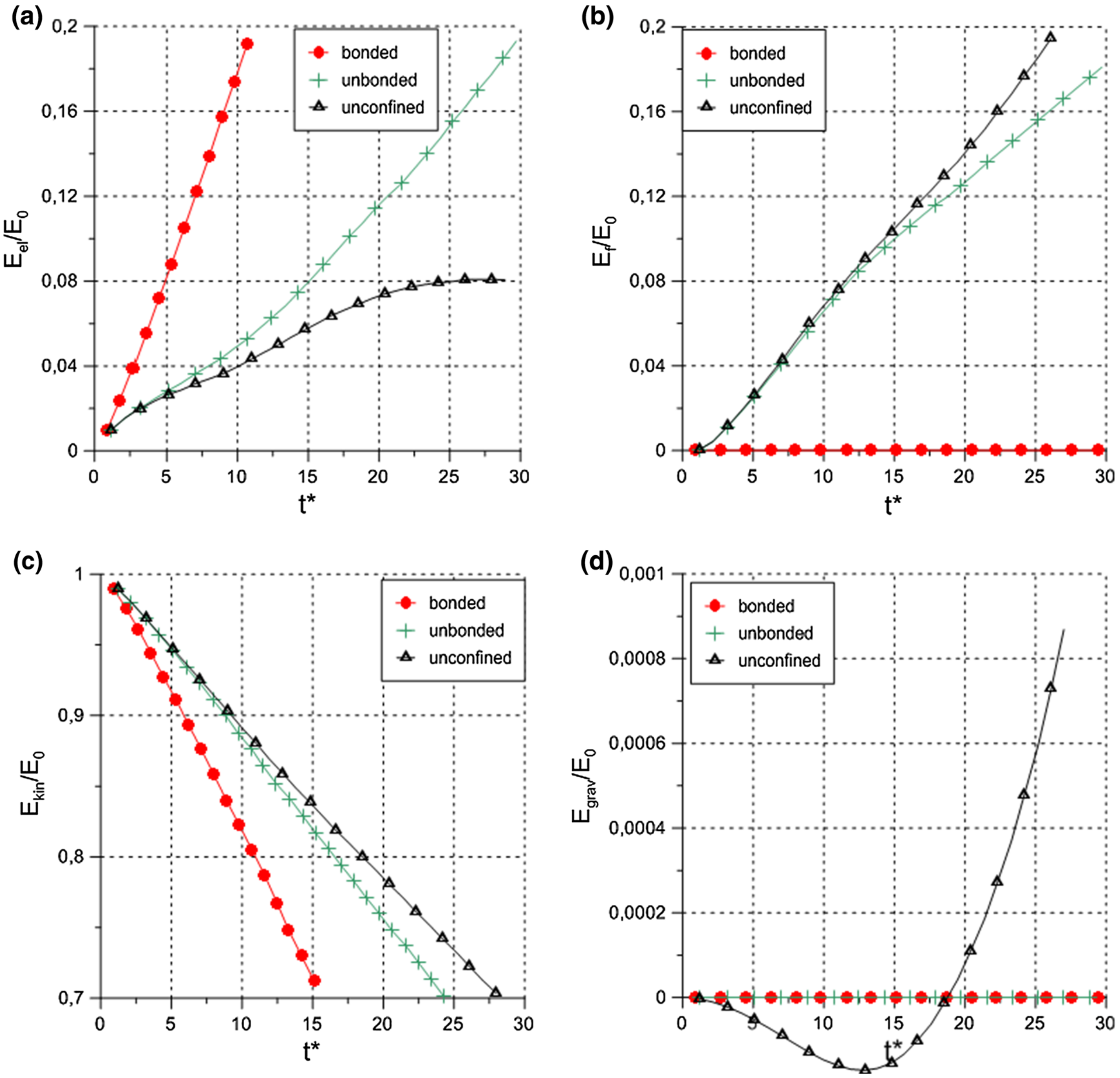

Fig. 11 Evolution of energy components; **a** elastic energy; **b** dissipated energy; **c** kinetic energy; **d** gravitational energy

In order to understand the reasons of the observed behaviour, it is useful to plot the evolution of the field of contact forces and particle velocities (Fig. 9).

The initial trend ($t^* < 5$) is identical to that of the confined flow, which is in agreement with the fact that impact forces are equal, too. In the following instants, two competing mechanisms are observed within the impacting mass: the backward propagation of the compression wave and the buckling of contact force chains. The latter starts from the top of the mass near the obstacle and propagates downward. In fact, a granular mass, which is not confined vertically, cannot bear static compressive stress horizontally. During the very first part of the impact, however, horizontal force chains can form, thanks to the inertia of grains that prevents their immediate displacement. In the following, a progressive misalignment of particles belonging to the same contact force chain occurs which reduces its capability of carrying a load. Therefore, the dynamically created compressive force chains becomes unstable, this resulting in the evident particles rearrangement by sliding and loss of contacts.

A similar effect was observed by Ceccato et al. [10, 11] who performed analogous simulations using the material point method and attributed the observed behaviour to the formation of vertically directed rarefaction waves. Correspondingly, in the affected region, particles are deflected upwards and maintain a horizontal component of velocity; in the same area, contact forces tend to zero. The impact wave transmission in the lower part of the mass is unaffected by buckling and reaches the back of the mass approximately at $t^* = 80$, as it was in the confined case. The adverse effect of buckling on force transmission within the mass is also witnessed by the fact that the maximum stored elastic energy is attained when the potential energy of the mass starts to increase (see Sect. 4.1 for a detailed analysis). At $t^* = 100$, the buckling effect has prevailed (i.e. it has propagated to the bottom of the granular mass): the contact force network has been destroyed, the impact force nullifies and dissipated energy comes to a steady value. However, a side effect of buckling is that the particles keep a positive horizontal velocity since the equivalent stiffness of the system is strongly reduced. As a consequence, contact forces form again, the impact force increases and a second wave of energy dissipation is observed. One or more sub-peaks (two in the case under consideration) may form as a consequence of the observed competing mechanisms. Note in general that the behaviour of the particles is much more disordered in the case of unconfined flow, and that the deformation of the mass is much larger.

3.4 Theoretical discussion

The comparison of impact forces obtained with the vertical front geometry is shown in Fig. 10.

The first value of the impact force is related to the interaction with the first line of grains in contact with the wall (for $\alpha = 90°$). The three curves in Fig. 10a, in fact, present the same initial value. After this first value, in case of confined flow and bonded particles, the value of the force increases because of the pressure exerted by the particles behind the first line and stabilises to the value corresponding to an elastic continuum of equivalent stiffness. On the contrary, in case of confined flow and frictional particles, the force decreases because the contact force transmission and the assembly equivalent stiffness are affected by particle sliding; in case of unconfined flow, a steep decrease in the impact force is observed due to the buckling effect.

The two confined tests give qualitatively similar results, characterised by a horizontal plateau followed by a rapid decrease. In both cases, a complete rebound of the mass is produced, with no residual force at the end of the impact. When the particles are bonded, the impact force is larger and the impact duration is shorter. All in all, the normalised impulse exerted on the barrier is larger when particles are bonded ($I^* = 7100$) with respect to the unbonded case ($I^* = 5250$), respectively, which is in agreement, as previously discussed, with the fact that the rebound velocity of the particles is larger. On the contrary, if the very first instants are excluded (see Figs. 6 and 9), the unconfined impact produces a completely different time evolution of the impact force, which decreases very rapidly. As a consequence, the impulse on the barrier is much smaller ($I^* = 1250$).

The analysis of the evolution of the energy components (Fig. 11) confirms that in the first instants, the two impacts with a purely frictional material (unbonded and unconfined curves) share a common behaviour in terms of elastic, dissipated and kinetic energy (Fig. 11a–c). The discrepancies become evident at about $t = 5^*$, when the upward displacements associated with buckling of contact force chains (Fig. 9) develop.

On the contrary, the evolution of the gravitational energy (Fig. 11d) is different: in the confined case, no gravity has been introduced and $E_{\text{grav}} = 0$. In the unconfined case, when $t^* < 13$, E_{grav} decreases and is negative. This is due to the fact that many particles are still moving downwards due to the effect of gravity. When $t^* > 13$, E_{grav} starts increasing very rapidly and becomes positive at

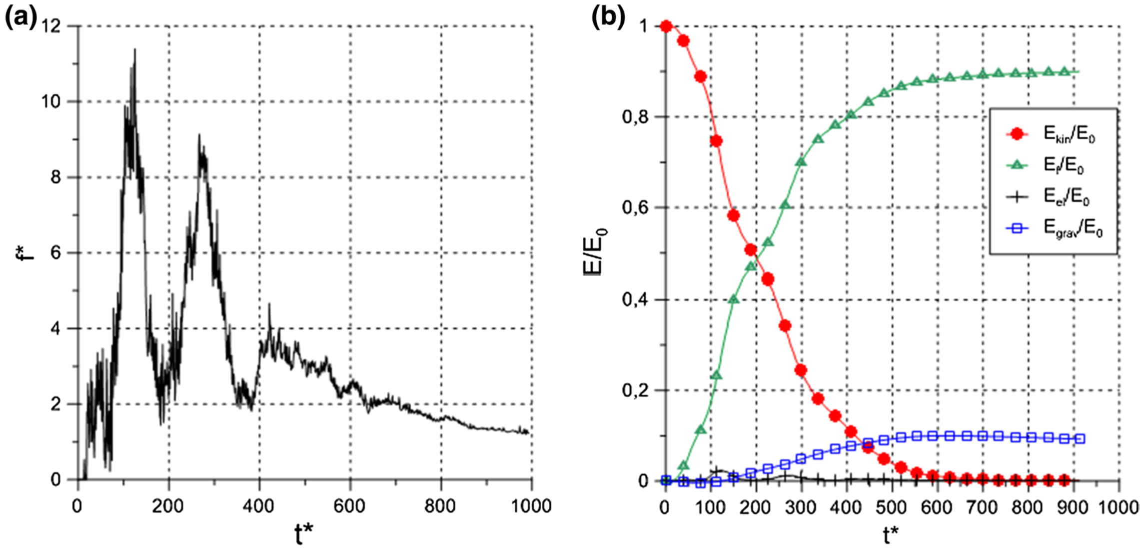

Fig. 12 Inclined front ($\alpha = 40°$). Evolution with time of: **a** normalised impact force; **b** normalised energy components E_{kin}, E_{el}, E_{f} and E_{grav}

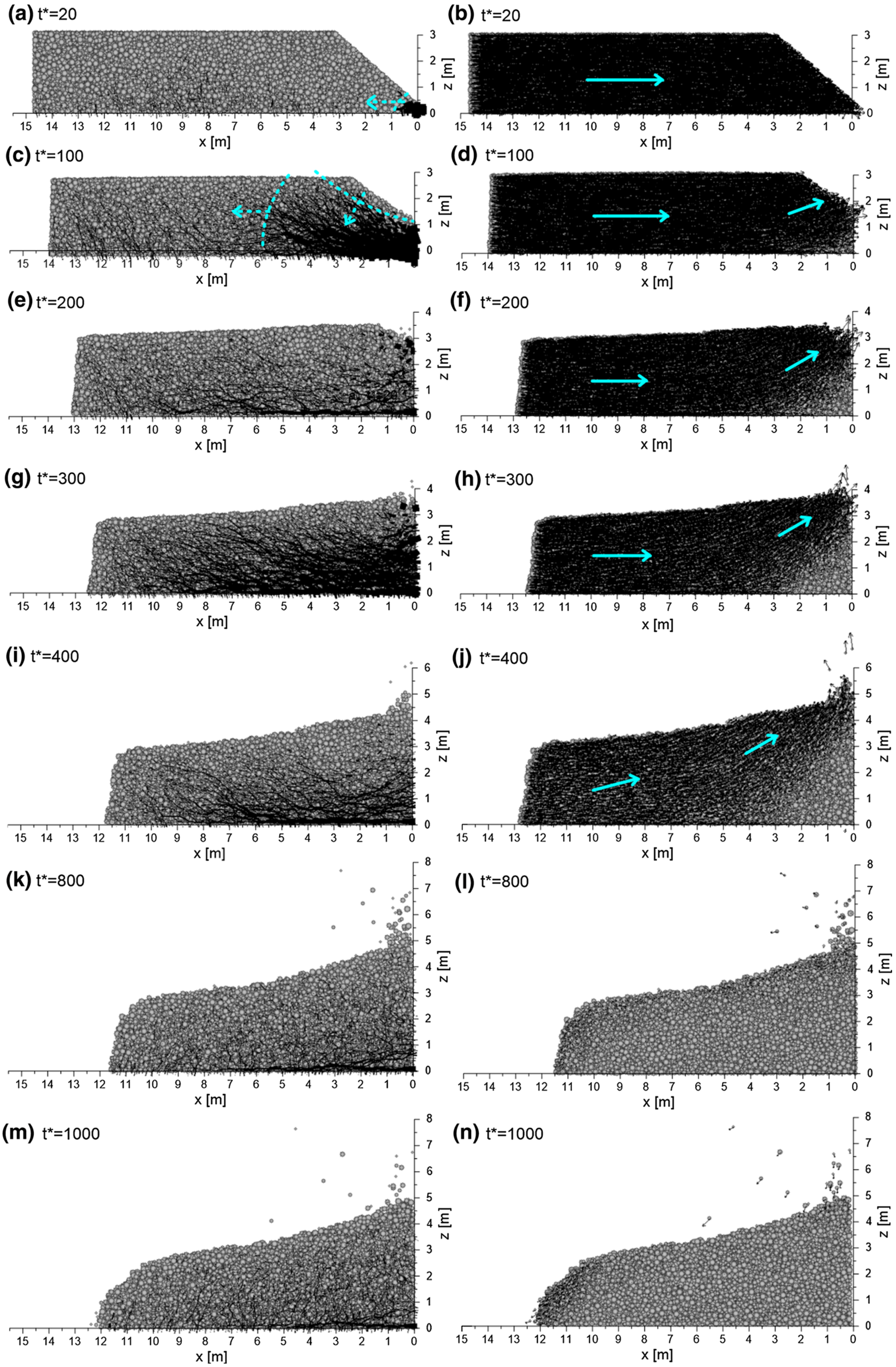

Fig. 13 Contact forces (left) and particle velocities (right) at selected time instants. Inclined front, free flow. The intensity of force chains is normalised with respect to 200 kN, whereas the intensity of the velocity vectors with respect to 8.8 m/s. Dashed arrows represent the moving direction of the wave front, whereas dashed lines represents the profile of the compression/rarefaction waves; solid arrows indicate the direction of the velocity vectors

t* = 17. This change in sign is due to the fact that at this stage, the upward displacement of particles dominates, due to the impact dynamic effect.

As was discussed in Sects. 3.1 and 3.2, the behaviour of the granular mass during confined impacts is similar to that of a deformable (elastic if bonds are present) body. The equivalent macroscopic properties of the granular mass can be evaluated from the velocity of propagation of the 1D impact wave C_D. This procedure is rigorous when the behaviour is elastic, but can be applied also to the unbonded case, provided that the elasto-plastic stiffness is employed.

Analysing data of Figs. 3, 4 (bonded material) and Figs. 6, 7 (purely frictional material) C_D are equal to 230 m/s and 140 m/s, respectively.

Considering that the bulk density of the material is $\rho = 1.43\ \mathrm{t/m^3}$ (see Table 1), the equivalent macroscopic confined stiffness of the bonded mass is therefore:

$$E_D = \rho C_D^2 = 75.6 \cong 76\ \mathrm{MPa} \tag{3}$$

The impact of a deformable body with such elastic properties would generate an impact stress:

$$\sigma_x = \rho C_D u_0 = 2.9\ \mathrm{MPa} \tag{4}$$

which is in good agreement with the numerical results (Fig. 4). This stress corresponds to a normalised impact force $f^* = 78$, which is in very good agreement with the numerical results (Fig. 10a, b).

Following the same approach used for the bonded mass, the equivalent macroscopic confined stiffness of the unbonded mass would be $E_D = 28.03 \cong 28$ MPa, and the corresponding a normalised impact force $f^* = 45$, which is in very good agreement with the numerical results (Fig. 10a, b). In terms of impulse, the elastic model ($I^* = 7200$) matches very well the numerical results obtained with the bonded material. The elastic model overestimates, as expected, the impulse obtained in the numerical simulation performed without bonds. In fact, the purely frictional mass undergoes a smaller momentum variation, because rebound velocity is smaller than impact velocity.

As a conclusion, the deformable body model seems to be both qualitatively and quantitatively appropriated for describing the confined impact of a bonded granular mass, provided that the equivalent stiffness is evaluated according to the observed impact wave velocity.

4 Numerical results: inclined front

4.1 Free surface flow, frictional material

The last series of simulations is performed by considering impacts where the front inclination α is between 30° and 80°. From a qualitative point of view, all these simulations share a similar behaviour. As a reference, the results obtained with α = 40° will be shown and qualitatively discussed in the following. Sect. 4.2 is devoted to the quantitative analysis of all impacts with inclined front.

The evolution of impact force with time in the case of inclined front and free surface is shown in Fig. 12 for α = 40°. The trend is quite irregular and is characterised by an initial increase until a peak is reached. In the following phases, the impact force tends to decrease, although secondary peaks are recorded. The overall duration of the impact is much longer than that in the case of vertical front,

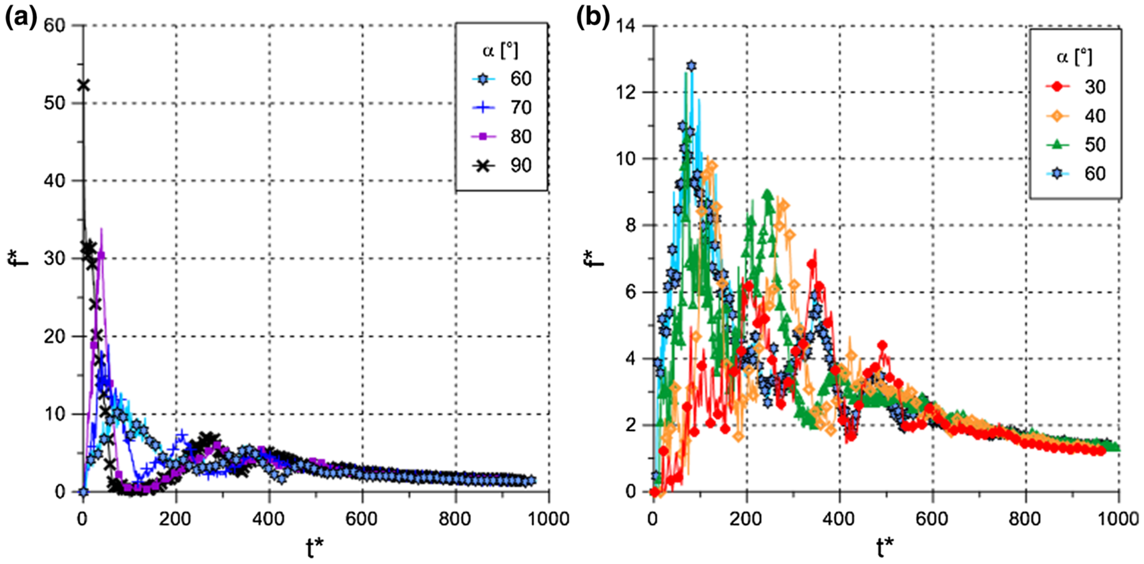

Fig. 14 Effect of front inclination α. Evolution of impact force with time; **a** α = 60–90°, **b** α = 30–60°

and the maximum impact force is much smaller. In terms of energy components, the observed trend is qualitatively similar to that observed for the vertical front. However, the maximum amount of stored elastic energy never exceeds 5% of the impact energy, in agreement with the fact that the impact force is much smaller than in the vertical front impact (see Sect. 4.2).

The evolution of the field of contact forces provides clarifying insights for explaining this behaviour (Fig. 13).

Three mechanisms are competing and determine the irregular trend observed in the impact force evolution with time: the wave propagation, the buckling and the progressive increase in the impact area, since the front particles do not hit the obstacle at the same time at which the force network regenerates. As a result, neither impact force nor contact forces within the mass go to zero during impact evolution with time (see also Sect. 4.2). Synthetically, each peak observed in the force–time curve is associated with a buckling phenomenon due to the compressive wave propagation within the soil mass.

From a purely qualitative point of view, it is also evident that in the case of inclined front, the impact is much more disordered, and the overall behaviour tends to be qualitatively more similar to that of a fluid.

4.2 Parametric analysis and theoretical discussion

The factors affecting the maximum value of impact force (f^*_{MAX}) were studied in a previous paper (Calvetti et al. [7]) where an appropriate design formula was proposed (Eq. 1 of this paper). However, as discussed in Sect. 1, impacts are dynamic phenomena and also the evolution with time of impact force should be considered for the design of protection works or the evaluation of vulnerability of existing structures.

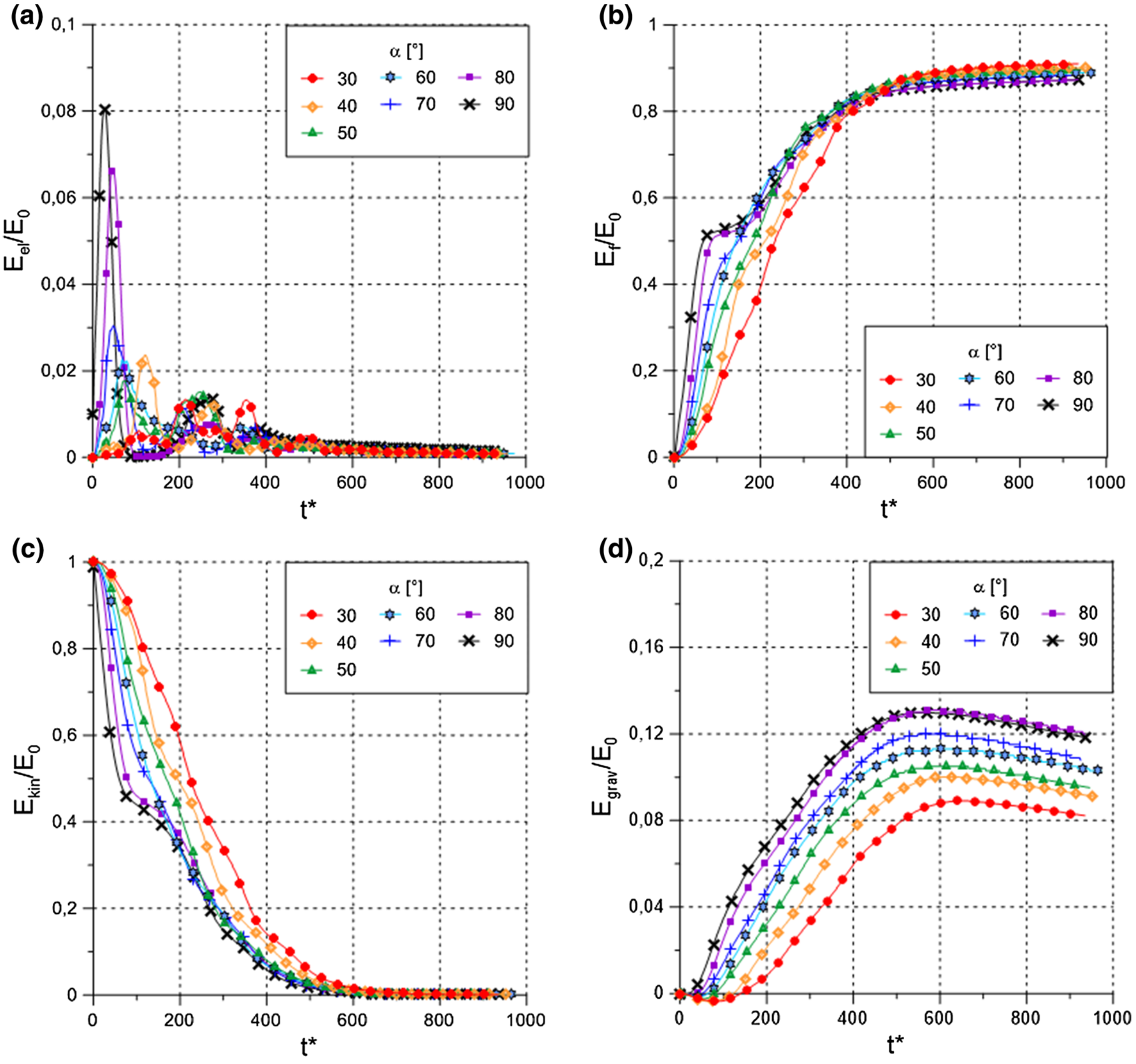

Fig. 15 Evolution of energy components; **a** elastic energy; **b** dissipated energy; **c** kinetic energy; **d** gravitational energy

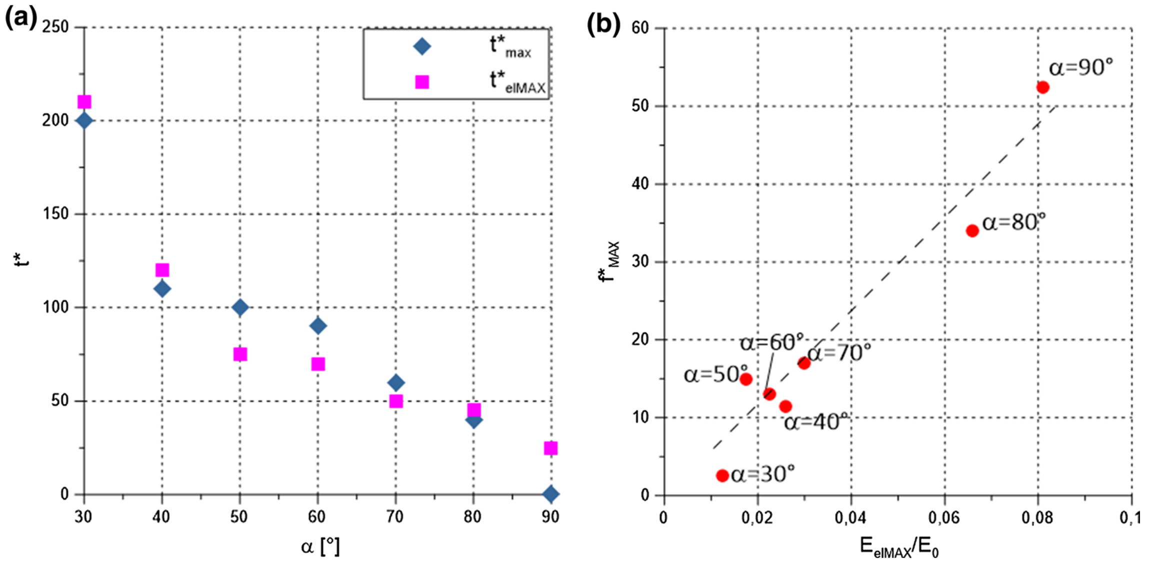

Fig. 16 Effect of front inclination. **a** Correlation between maximum elastic energy and maximum impact force (front inclination in the labels); **b** time at peaks of impact force and stored elastic energy

The evolution of impact force with time is shown in Fig. 14 for all considered front inclinations ($\alpha = 30°–90°$). The following trends are observed for a decrease in the front inclination: (i) the maximum impact force decreases (Calvetti et al. [7], and Fig. 16a); (ii) the time instant when the maximum impact force attained is progressively delayed (Fig. 16b); (iii) secondary peaks become more relevant with respect to the first one; the number of relevant secondary peaks increases; the oscillation of the impact force between two peaks becomes smaller.

All impacts are characterised by a similar final evolution: major oscillations of the impact force disappear at $t^* = 600$ and all curves converge to a common trend, irrespectively of the initial front inclination. Then, f^* slowly decreases, and a residual force equal to 1.5 is attained for $t^* = 900$.

The evolution of energy components with time is shown in Fig. 15. The maximum values of E_{el} and E_{grav} are approximately 10% of the impact energy, E_0. The main energy exchange mechanism is therefore that E_{kin} is progressively transformed into E_{f}, i.e. dissipated by friction. As a consequence, the trends of E_{f} and E_{kin} are clearly connected and both exhibit a peculiar plateau for $\alpha = 80°$ and 90°. This corresponds to the instant of time at which the contact force network is completely disrupted ($t^* = 100$, see Fig. 9), and as a consequence, no energy dissipation can occur. The plateau tends to disappear for shallower inclinations, i.e. when the mechanism of progressive impact at the front becomes more relevant and regenerates the force network. In fact, for $\alpha \leq 70°$, the minimum impact force never nullifies.

At the end of the impacts, kinetic energy is zero in all cases and the initial energy has been either dissipated or transformed into gravitational energy. E_{f} is about 90% of the impact energy, and only slightly decreases with the front inclination. E_{grav} is about 10% of the impact energy, and only slightly increases with the front inclination (which exactly compensates the differences in term of dissipated energy).

The trend of E_{el} is qualitatively very similar to that of the impact force (Figs. 14 and 15a). The connection between these variables is quantitatively confirmed by the data of Fig. 16. Not only f^*_{MAX} is strictly correlated with E_{elMAX} (Fig. 16a), but also the time instants corresponding to E_{elMAX} and f^*_{MAX} are very close to each other (Fig. 16b). In fact, the maximum of the impact force corresponds to the development of force chains within the granular mass, and for this reason, it is related to the maximum value of storage of the elastic energy. Figure 16b also quantitatively shows that the time interval before the maximum force is attained and decreases with front inclination.

5 Conclusions

In this paper, the impact of a granular mass on a rigid obstacle is analysed from both a micromechanical and global (macroscopic) point of view.

The correlation between macroscopic variables (impact force) and local information (contact forces, particle velocities) allows to highlight the mechanisms responsible for the complex macroscopic behaviour. In particular, three concurring (in part competing) processes have been put in evidence: the propagation of compression and no-tension waves within the mass; the buckling effect; the increase in the contact area between the mass and the obstacle. Impact geometry has a clear effect on the mutual relevance of these three factors, and it also determines qualitatively different deformation processes which are similar to that of a solid for confined impacts and vertical fronts, and to that of a fluid for inclined fronts. In terms of maximum impact force, these considerations justify the need for the formula previously introduced by the authors, where both solid body and hydrodynamic components are included with a relative importance depending on the mentioned factors.

The elastic body model is both qualitatively and quantitatively suitable only when the unrealistic case of confined impact and bonded material is considered. This model can also be used for confined impacts of a purely frictional mass, provided that the equivalent stiffness is evaluated on the basis of the observed (elasto-plastic) impact wave velocity, but some noticeable discrepancies arise, in terms of impact duration and overall impulse.

If the flow is not confined, the elastic model is not suitable: the dissipated energy is much larger than the stored elastic energy, at any time instant during the impact. In fact, the elastic body model contains only information required for describing wave transmission, which is just one of the three highlighted processes.

From a design point of view, the results integrate the formula that was previously introduced for f^*_{MAX}, by adding information about the time evolution of the impact force. In particular, results show that the time duration of impacts and the residual value of the impact force are almost unaffected by the front inclination. On the contrary, the time at peak of the impact force is clearly decreasing with front inclination.

Acknowledgements Irene Redaelli is supported by a fellowship from Fondazione Cariplo, Grant no. 2016-0769.

References

1. Albaba A, Lambert S, Faug T (2017) Dry granular avalanche impact force on a rigid wall of semi-infinite height. In: EPJ web of conferences, vol 140. EDP Science, p 03054
2. Ahmadipur A, Qiu T (2018) Impact force to a rigid obstruction from a granular mass sliding down a smooth incline. Acta Geotech 13(6):1433–1450
3. Arattano M, Franzi L (2003) On the evaluation of debris flows dynamics by means of mathematical models. Nat Hazards Earth Syst Sci 3(6):539–544
4. Armanini A (1997) On the dynamic impact of debris flows. In: Recent developments on debris flows. Springer, Berlin, pp 208–226. https://doi.org/10.1007/BFb0117757
5. Bugnion L, McArdell BW, Bartelt P, Wendeler C (2012) Measurements of hillslope debris flow impact pressure on obstacles. Landslides 9(2):179–187
6. Calvetti F (2008) Discrete modelling of granular materials and geotechnical problems. Eur J Environ Civ Eng 12(7–8):951–965
7. Calvetti F, di Prisco C, Vairaktaris E (2017) DEM assessment of impact forces of dry granular masses on rigid barriers. Acta Geotech 12(1):129–144
8. Calvetti F, di Prisco C, Vairaktaris E (2016a) Debris flow impact forces on rigid barriers: existing practice versus DEM numerical results. In: Proceedings of ICONHIC 2016, Chania, p 1–14
9. Calvetti F, di Prisco C, Vairaktaris E (2016b) Dry granular flows impacts on rigid obstacles: DEM evaluation of a design formula for the impact force. In: Proceedings of 6th Italian conference of researchers in geotechnical engineering, Bologna, p 290–295
10. Ceccato F, Simonini P, di Prisco C, Redaelli I (2017) The effect of the front inclination on the impact forces transmitted by granular flows to rigid structures. In: Proceedings 4th world landslide forum, Ljubljana, p 593–600
11. Ceccato F, Redaelli I, di Prisco C, Simonini P (2018) Impact forces of granular flows on rigid structures: comparison between discontinuous (DEM) and continuous (MPM) numerical approaches. Comput Geotachnics 103:201–217. https://doi.org/10.1016/j.compgeo.2018.07.014
12. Cundall PA, Strack OD (1979) A discrete numerical model for granular assemblies. Geotechnique 29(1):47–65
13. De Blasio FV (2011) Introduction to the physics of landslides. Springer, Berlin
14. Dok L (2000) Review of natural terrain landslide debris-resting barrier design, Geotechnical Engineering Office. Geo Report No. 104. Civil Engineering Department: Government of the Hong Kong Special Administrative Region
15. Hong Y, Wang JP, Li DQ, Cao ZJ, Cui P (2015) Statistical and probabilistic analyses of impact pressure and discharge of debris flow from 139 events during 1961 and 2000 at Jiangjia Ravine, China. Eng Geol 187:122–134
16. Huang HP, Yang KC, Lai SW (2007) Impact force of debris flow on filter dam. In: Geophysical research abstracts, vol 9, p 03218. https://gra103.aca.ntu.edu.tw/gdoc/96/D91622005a.pdf. Accessed 2 May 2013
17. Hübl J, Suda J, Proske D, Kaitna R, Scheidl C (2009) Debris flow impact estimation. In: Proceedings of the 11th international symposium on water management and hydraulic engineering, Ohrid, Macedonia 1:137–148
18. Ishikawa N, Inoue R, Hayashi K, Hasegawa Y, Mizuyama T (2008) Experimental approach on measurement of impulsive fluid force using debris flow model. In: Conference proceedings interpraevent, vol 8
19. Itasca (2011) PFC3D, theory and background. Itasca, Minneapolis
20. Jóhannesson T, Gauer P, Issler P, Lied K, Hákonardóttir KM (2009) The design of avalanche protection dams: recent practical and theoretical developments. European Commission, Climate Change Research-Series 2 Project report, EUR 23339
21. Kwan JSH (2012) Supplementary technical guidance on design of rigid debris-resisting barriers. Geotechnical Engineering Office, HKSAR. GEO Report, (270)
22. Li X, Zhao J (2018) A unified CFD-DEM approach for modeling of debris flow impacts on flexible barriers. Int J Numer Anal Methods Geomech 1:2–3. https://doi.org/10.1002/nag.2806
23. Neto AHF, Borja RI (2018) Continuum hydrodynamics of dry granular flows employing multiplicative elastoplasticity. Acta Geotech 13(5):1027–1104
24. Prochaska AB, Santi PM, Higgins JD, Cannon SH (2008) A study of methods to estimate debris flow velocity. Landslides 5(4):431–444
25. Redaelli I, di Prisco C, Vescovi D (2016) A visco-elasto-plastic model for granular materials under simple shear conditions. Int J Numer Anal Meth Geomech 40(1):80–104

26. Rickenmann D (1999) Empirical relationships for debris flows. Nat Hazards 19(1):47–77
27. Scotton P, Deganutti AM (1997) Phreatic line and dynamic impact in laboratory debris flow experiments. In: Debris-flow hazards mitigation: mechanics, prediction, and assessment ASCE, 777–786
28. Suda J, Hübl J, Bergmeister K (2010) Design and construction of high stressed concrete structures as protection works for torrent control in the Austrian Alps. In: Proceedings of the 3rd fib international congress, Washington, USA, p 1–8
29. Shen W, Zhao T, Zhao J, Dai F, Zhou GG (2018) Quantifying the impact of dry debris flow against a rigid barrier by DEM analyses. Eng Geol 241:86–96
30. Teufelsbauer H, Wang Y, Pudasaini SP, Borja RI, Wu W (2011) DEM simulation of impact force exerted by granular flow on rigid structures. Acta Geotech 6(3):119
31. Zhang S (1993) A comprehensive approach to the observation and prevention of debris flows in China. Nat Hazards 7(1):1–23